of 3D periodic mesostructured materials without assuming any structural models. The resolution for the structure is primarily limited by the quality of the HREM images, which depends on the long-range mesoscale ordering. Therefore, although further progress may give better resolution, we expect no future change to the present conclusions about the structures of SBA-1, SBA-6 and SBA-16, because the validity of the solutions does not depend on the resolution. This is a characteristic of our method that makes it different from other approaches. We also suggest that the results presented here provide a quantitative topological description of ordered mesostructured composites, and that such descriptions are essential in understanding the properties and possible applications of the composites. The resolution of periodically ordered, 3D arrangements of bimodal (meso-micro) pores in SBA-1 and SBA-6 makes it possible to consider the detailed characterization of the range of complicated porous phases that are now synthetically achievable. □

Methods

Synthesis of SBA-6

3.75 g of tetraethoxysilane (TEOS) was added with magnetic stirring to a clear solution containing 0.5 g of the gemini surfactant $18B_{4\text{-}3\text{-}1}$ (N,N,N,N′N′-pentamethyl-N′-[4-(4-octadecyloxyphenoxy)-butyl]-propane-1,3-diammonium dibromide, $C_{18}H_{37}OC_6H_4OC_4H_8N(CH_3)_2C_3H_6N(CH_3)_3Br_2$), 45.4 g of doubly distilled water, and 3.69 g of benzyltrimethylammonium hydroxide at room temperature. Stirring was continued for 20 h after the addition of TEOS at room temperature. The reaction gel mixture was heated for 2 d at 80 °C without stirring. The precipitate was filtered and dried in air at room temperature.

Determination of properties

Ar adsorption and desorption isotherms were measured at 87 K. Pore volumes ($cm^3\,g^{-1}$) for SBA-1, SBA-6 and SBA-16 are 0.6, 0.86 and 0.45, respectively, and the ratios of the pore volume to unit cell are respectively 0.57, 0.65 and 0.47. The surface-area/pore-volume ratio ($2.26 \times 10^9\,m^{-1}$) for SBA-1 is nearly three times that of SBA-6 ($7.93 \times 10^8\,m^{-1}$). The silica wall densities determined with an AccPyc 1300 helium pycnometer are also substantially different for SBA-1 ($2.00\,g\,cm^{-3}$) and SBA-6 ($2.20\,g\,cm^{-3}$).

Received 23 May; accepted 6 October 2000.

1. Zhao, D. *et al.* Triblock copolymer syntheses of mesoporous silica with periodic 50 to 300 Ångstrom pores. *Science* **279,** 548–552 (1998).
2. Zhao, D., Huo, Q., Feng, J., Chmelka, B. F. & Stucky, G. D. Nonionic triblock and star diblock copolymer and oligomeric surfactant syntheses of highly ordered, hydrothermally stable, mesoporous silica structures. *J. Am. Chem. Soc.* **120,** 6024–6036 (1998).
3. Alfredsson, V. & Anderson, M. W. Structure of MCM-48 revealed by transmission electron microscopy. *Chem. Mater.* **8,** 1141–1146 (1996).
4. Monnier, A. *et al.* Cooperative formation of inorganic-organic interfaces in the synthesis of silicate mesostructures. *Science* **261,** 1299–1303 (1993).
5. Schacht, S., Janicke, M. & Schüth, F. Modeling X-ray patterns and TEM images of MCM-41. *Microporous Mesoporous Mater.* **22,** 485–493 (1998).
6. Huo, Q. *et al.* Generalized syntheses of periodic surfactant/inorganic composite materials. *Nature* **368,** 317–321 (1994).
7. Huo, Q. *et al.* Organization of organic molecules with inorganic molecular species into nanocomposite biphase arrays. *Chem. Mater.* **6,** 1176–1191 (1994).
8. Auvray, X. *et al.* X-ray diffraction and freeze-fracture electron microscopy study of the cubic phase in the cetylpyridinium chloride formamide and cetyltrimethylammonium chloride formamide systems. *Langmuir* **9,** 444–448 (1993).
9. Charvolin, J. & Sadoc, J. F. Periodic systems of frustrated fluid films and "micellar" cubic structures in liquid crystals. *J. Phys. France* **49,** 521–526 (1988).
10. Ryoo, R., Kim, J. M. & Ko, C. H. in *Studies in Surface Science and Catalysis* Vol. 117 (eds Bonneviot, L., Béland, F., Danumah, C., Giasson, S. & Kaliaguine, S.) 151–158 (Elsevier, Amsterdam, 1998).
11. Nakanishi, K. Pore structure control of silica gels based on phase separation. *J. Porous Mater.* **4,** 67–112 (1997).
12. Geis, H. Studies on clathrasils. III. Crystal structure of melanophlogite, a natural clathrate compound of silica. *Z. Kristallogr.* **164,** 247–257 (1983).

Supplementary Information is available on *Nature*'s World-Wide Web site (http://www.nature.com) or as paper copy from the London editorial office of *Nature*.

Acknowledgements

This work was supported in part by CREST, Japan Science and Technology Corporation (O.T.), by the National Research Laboratory Program of Korea (R.R.), and by the National Science Foundation (G.D.S.) and the Army Research Office (G.D.S.). O.T. thanks S. Andersson for encouragement and support. Y.S. thanks the Japan Society for the Promotion of Science.

Correspondence and requests for materials should be addressed to O.M. (e-mail: terasaki@msp.phys.tohoku.ac.jp) or R.R. (e-mail: r.ryoo@mail.kaist.ac.kr).

Improved estimates of global ocean circulation, heat transport and mixing from hydrographic data

Alexandre Ganachaud* & Carl Wunsch

MIT 54-1517, 77 Massachusetts Avenue, Cambridge, Massachusetts 02139, USA

Through its ability to transport large amounts of heat, fresh water and nutrients, the ocean is an essential regulator of climate[1,2]. The pathways and mechanisms of this transport and its stability are critical issues in understanding the present state of climate and the possibilities of future changes. Recently, global high-quality hydrographic data have been gathered in the World Ocean Circulation Experiment (WOCE), to obtain an accurate picture of the present circulation. Here we combine the new data from high-resolution trans-oceanic sections and current meters with climatological wind fields, biogeochemical balances and improved a priori error estimates in an inverse model, to improve estimates of the global circulation and heat fluxes. Our solution resolves globally vertical mixing across surfaces of equal density, with coefficients in the range $(3\text{–}12) \times 10^{-4}\,m^2\,s^{-1}$. Net deep-water production rates amount to $(15 \pm 12) \times 10^6\,m^3\,s^{-1}$ in the North Atlantic Ocean and $(21 \pm 6) \times 10^6\,m^3\,s^{-1}$ in the Southern Ocean. Our estimates provide a new reference state for future climate studies with rigorous estimates of the uncertainties.

Obtaining a consistent picture of the oceanic circulation requires adjusting thousands of parameters consistently with a priori error estimates. We present here our best estimate from selected hydrographic data (Fig. 1), which will improve with the appearance of new data. Mass flux is the most basic element of the circulation and Fig. 2 shows the best-estimate coast-to-coast integrated water mass transports for selected density classes. A volume of 15 ± 2 Sv (1 sverdrup $= 1 \times 10^6\,m^3\,s^{-1}$) of North Atlantic Deep Water (NADW) is produced in the northern North Atlantic Ocean and moves southward, entraining Antarctic Bottom Water (AABW) from below, and Antarctic Intermediate Water (AAIW) from above. As a result, the NADW is increased to 23 ± 3 Sv as it exits the South Atlantic at 30° S. In the Southern Ocean, a total of 21 ± 6 Sv of bottom water is formed from lower Circumpolar Deep Water (CDW)—which corresponds approximately to the lower NADW density range. Bottom water inflows (NADW + AABW mixture) to the Atlantic, Indian and Pacific oceans are 6 ± 1.3 Sv, 11 ± 4 Sv and 7 ± 2 Sv, respectively. In the Indian and Pacific oceans, most of this water returns southward at deep and intermediate levels. These net values are the sums of large, strongly spatially varying, flows of opposing sign, and thus oversimplify the actual circulation; a detailed description of the circulation within each ocean basin will be published elsewhere[3,4]. Our standard model estimate of the inflow in the South Pacific Ocean is in the lower range of previously published values, but it depends directly upon the weight given to the "PO" phosphate–oxygen combination (see Methods[4,5]) conservation constraints relative to mass conservation[3]. The deep inflow to the North Pacific Ocean is also weaker than previously found[5], as a consequence of our consideration of heat and salt conservation in the northern parts of those basins.

No definition of bottom-water formation can be completely unambiguous because of the entrainment of ambient fluid during the sinking process. In our Southern Ocean definition, the bottom-

* Pressent address: Laboratoire de Physique des Océans, IFREMER, 29280 Plouzané, France.

water formation rate corresponds to the total amount of water crossing the neutral surface, $\gamma^n = 28.11\,\mathrm{kg\,m^{-3}}$ downwards, and subsequently ventilating the deep Atlantic, Indian and Pacific basins. This water is provided primarily from the density range of lower NADW, so that the two sources of deep water are not additive, as is often assumed in qualitative calculations[6]. Consistent with conventional wisdom, no very large amount of deep water forms in the North Pacific or Indian oceans, although intermediate waters are produced there. Transient tracer measurements suggest AABW formation rates of water denser than $\gamma^n = 28.27\,\mathrm{kg\,m^{-3}}$ at 5 to 8 Sv (ref. 7). Because this density class is almost immediately mixed with CDW above it when exiting the Southern Ocean, it is not separately resolved in our model, and there is no inconsistency. However, there is a contradiction with the suggestion that the current production rate of AABW recently decreased[6], as we find no inconsistency between the deep, contemporary, geostrophic circulation and the interior tracer field which reflects the circulation integrated over hundreds of years. We believe that the origin of the disagreement is in those authors' *ad hoc* assumptions[6] about the originating water masses.

The integrated circulation in the upper layers is more uncertain (Fig. 2, red arrows) owing to the enhanced temporal variability known to be present there[3]. A northward flow of 16 ± 3 Sv of thermocline water from the South Atlantic Ocean balances the NADW southward flow; the strength of the Pacific-Indonesian throughflow is estimated at 16 ± 5 Sv, consistent with the most recent current-meter measurements[8]. This estimate is sensitive to the use of hydrography at very low latitudes where noise susceptibility and seasonal variability are large.

Vertical exchanges (advection, denoted w^*, and mixing, measured by a diffusion coefficient κ^* across the neutral surfaces[9] defining the layers) are associated with the general circulation. Both parameters are now the focus of intense research[10,11] because numerical models are known to be very sensitive to κ^*. Direct measurements have shown little mixing in the ocean interior, while enhanced mixing of order $1{,}000\,\mathrm{cm^2\,s^{-1}}$ has been observed in oceanic regions with rough topography[11]. Table 1 summarizes the abyssal dianeutral (near vertical) exchanges by basin and depth range. Let an overbar denote a basin average. Then, in the deep range ($\simeq$2,000–3,500 m), dianeutral velocities are $\overline{w^*} = (0.1\text{–}0.6) \times 10^{-6}\,\mathrm{m\,s^{-1}}$, and the diffusivities are $\overline{\kappa^*} = (3\text{–}4) \times 10^{-4}\,\mathrm{m^2\,s^{-1}}$ with global averages of $\overline{w^*} = (0.13 \pm 0.03) \times 10^{-6}\,\mathrm{m\,s^{-1}}$ and $\overline{\kappa^*} = (3.7 \pm 0.7) \times 10^{-4}\,\mathrm{m^2\,s^{-1}}$ between 30° S and 47° N. In the bottom layers ($\simeq$3,800 m to the bottom), both means are larger: $\overline{w^*} = (0.4 \pm 0.1) \times 10^{-6}\,\mathrm{m\,s^{-1}}$ and $\overline{\kappa^*} = (9 \pm 2) \times 10^{-4}\,\mathrm{m^2\,s^{-1}}$. Diffusivity values in the deep range are consistent with previous calculations from a crude one-dimensional global balance[10]. The largest values are found in the bottom layers although they are correspondingly more uncertain[3]. The spatial average values that are required by our tracer balance result from all mixing processes, including probable strong mixing generated near topography[10,11]. We interpret those values[10] as being the basin-average value of a process strongly mixing the ocean at highly localized regions.

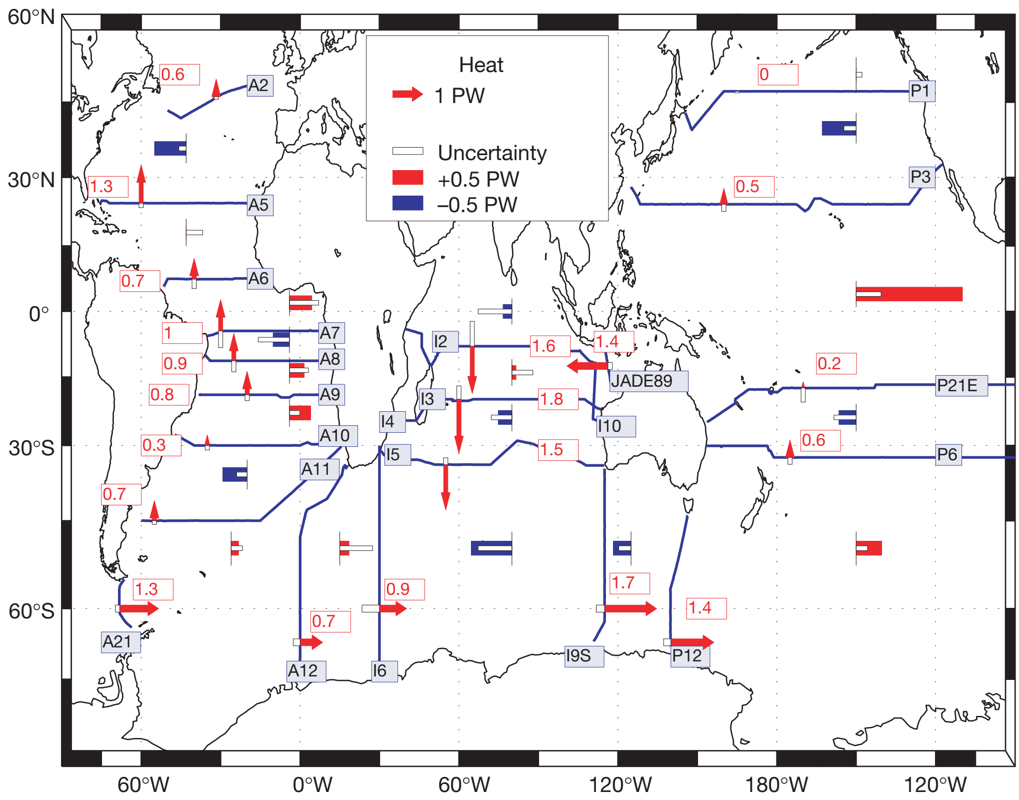

Figure 1 Hydrographic sections and heat fluxes. Transoceanic sections from the WOCE program were selected to ensure a reasonable temporal consistency (1990–1996) and to avoid crossing sections. Between Jakarta and Australia, the 1989 section from the Franco-Indonesian JADE program was used while pre-WOCE sections (1985, 1987)[3] were used in the North Pacific and at 32° S in the Indian Ocean. Each section is a collection of high-density temperature, salinity, oxygen and nutrient measurements. From temperature and salinity, a geostrophic velocity field is calculated and adjusted so that mass and other conservative tracers (see Methods) are conserved between sections. The resulting heat (or 'enthalpy', where the net mass flux is non-zero) transports are indicated by the arrows and red numbers (positive northward/eastward). The white box at the tail end of each arrow is the one-standard-deviation uncertainty. Between sections, ocean–atmosphere heat transfers are indicated by the zonal length of the coloured boxes (blue for ocean cooling; red for ocean heating), with the length of the white box inside indicating the uncertainty. (Because the ocean–atmosphere heat transfers are anomaly residuals, that is, corrected for residual mass imbalances, they do not correspond exactly to the differences between net fluxes across sections, for example, in the North Indian Ocean. But this discrepancy is much less than the uncertainties.)

Diffusivities could not be resolved in the Southern Ocean, where many neutral surfaces outcrop. The improved inverse model method has produced the first near-global, resolved estimates of the dianeutral transfers. The overall results are inconsistent with recent suggestions that the ocean mixes primarily at near-surface outcrops of the neutral surfaces, that is, primarily in the Southern Ocean[12]. Strong abyssal mixing is required by the observed geostrophically balanced circulation, and its absence is incompatible with the observed property distributions.

Figure 1 shows the heat (actually, enthalpy) transports, across each hydrographic section (arrows) along with the residuals reflecting atmospheric heat exchanges (boxes). Residuals are accurately determined at middle and high latitudes, but are more uncertain at lower latitudes (for example, in the Atlantic Ocean) owing to an enhancement of the geostrophic noise there[3]. Nevertheless, the total heating over the tropical Atlantic and Pacific oceans are well-determined, respectively 0.7 ± 0.2 PW ($1\,\mathrm{PW} = 10^{15}$ W) and 1.6 ± 0.4 PW. No significant heat transfers are found in the Indian Ocean because of the large, uncertain, warm water inflow from the Pacific Ocean. This large warm water flux is the main heat escape from the Pacific Ocean, resulting in a northward heat flux in the South Pacific. In the southern Pacific sector, significant heating is found, in contrast with the sparse *in situ* observations[13], but in qualitative agreement with the recent re-analysis of the European Centre for Medium Range Weather Forecasts[14]. Figure 3 shows the globally integrated heat fluxes compared to independent estimates. Most of the cooling occurs in the Northern Hemisphere, at a rate of -1.7 ± 0.2 PW, in balance with the 2.3 ± 0.4 PW heating in the tropical band and the -0.7 ± 0.3 PW cooling in the Southern Ocean.

Changes in the oceanic heat transport can have a large impact on atmospheric temperature gradients[15,16] and thus on climate. Previous estimates of the ocean–atmosphere heat exchanges that are based upon purely ocean surface observations are highly uncertain[17,18]. Analyses from numerical weather prediction centres provide oceanic surface fluxes that are often used as boundary conditions for driving ocean models, but associated uncertainty estimates are not provided. Heuristic calculations suggest uncertainties in their estimates of at least ± 0.6 PW for the meridional oceanic heat transport at most latitudes[19]. The present inversion indicates uncertainties that depend on latitude, with a high accuracy of globally integrated heat transfers (Fig. 3). Similar budgets, to be

Table 1 Basin-averaged dianeutral velocities and diffusivities

	$\overline{w*}$ ($10^{-6}\,\mathrm{m\,s^{-1}}$)	$\overline{\kappa*}$ ($10^{-4}\,\mathrm{m^2\,s^{-1}}$)
Atlantic bottom	0.5 ± 0.2	9 ± 4
Indian bottom	0.6 ± 0.3	12 ± 7
Pacific bottom	0.4 ± 0.1	9 ± 2
Southern bottom	-0.25 ± 0.1	–
Atlantic deep	0.1 ± 0.05	3 ± 1.5
Indian deep	0.3 ± 0.15	4 ± 2
Pacific deep	0.1 ± 0.03	4 ± 1
Southern deep	0.1 ± 0.1	–

The average is calculated on neutral surfaces from $\gamma^n = 28.1\,\mathrm{kg\,m^{-3}}$ to the bottom (generally 3,800 decibars (or metres) to the bottom) for the 'bottom layers' and from $\gamma^n = 27.96$ to $\gamma^n = 28.07$ for the 'deep layers' (generally 2,000 m to 3,500 m).

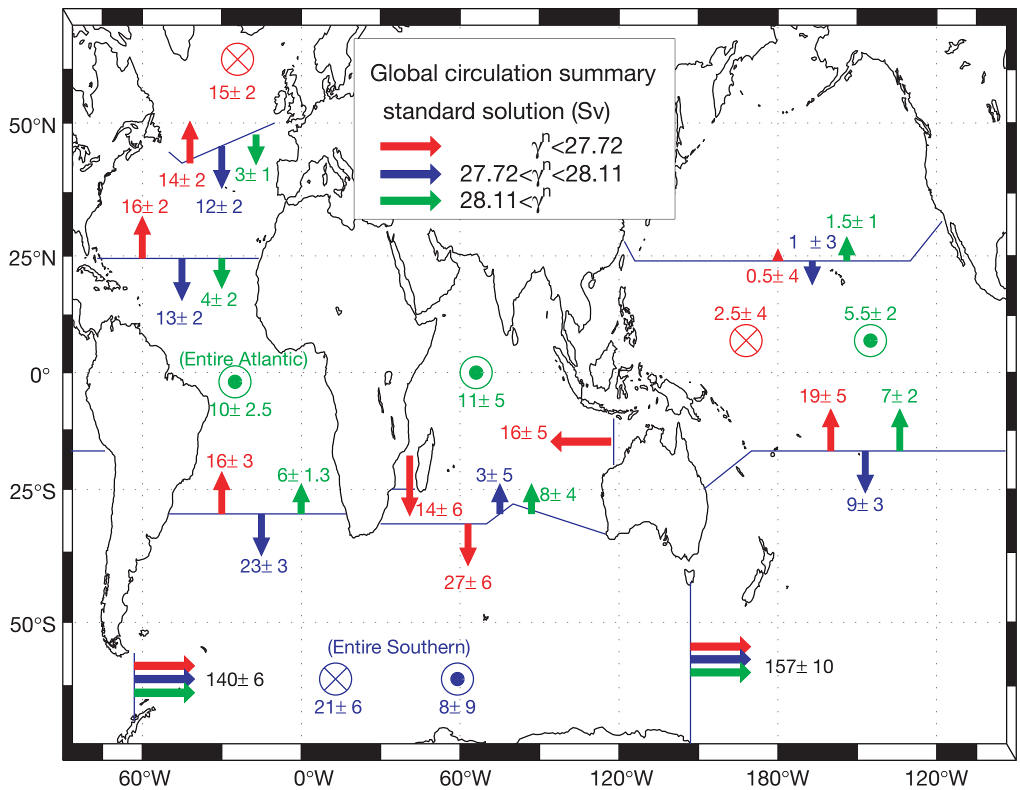

Figure 2 Zonally integrated layer mass transports. The estimated water transports are indicated for the different density classes bounded by neutral surfaces (γ^n, in kg m^{-3}) and across selected hydrographic sections. Neutral surfaces are close to surfaces of constant density, but are chosen so that movement along them minimizes the work done against gravity. The colour of the upwelling or down-welling arrows indicates the layer from which the water is coming. A flux of 0.8 Sv from the Pacific to the Atlantic Ocean through the Bering Strait was taken into account, although it is much smaller than the uncertainties on the net transports. In the Southern Ocean, the bottom water formation takes place mostly in the Weddell Sea, while the upwelling distribution is uncertain. In the Indian Ocean, most of the upwelling takes place north of 7° S. The South Pacific transports are given at 17° S because of the more complicated structure at 32° S (ref. 3). Note the increase in the Southern Ocean transport south of Australia owing to the recirculation of Indonesian throughflow water.

published elsewhere, of oxygen and nutrients, are important for both climate and biogeochemical processes[3,20].

The physical circulation estimated here during WOCE provides a new reference state for climate change studies, and a test—within the estimated uncertainties—of general circulation models of both atmosphere and ocean. The estimated values of κ^* and w^* represent values that models will need to simulate. The high-resolution WOCE data set, the confinement in time, the use of current-meter data as constraints in boundary currents, and the detailed analysis of the uncertainties associated with our method are great improvements in reliability over previous circulation estimates. Within the error estimates, there is no conflict in either transports or heat fluxes with a previous global inversion that was based on a nearly independent and coarser data set[1,21], and no statistically significant change in integrated mass transports over the past 30 years was found[1,22]. This is an important conclusion in its own right.

Improving the accuracy of the estimates made from the present data sets, if interpreted as climatological averages, will not be easy. Although the addition of new data, for example, existing or future meridional sections, will better the spatial resolution, limitations now lie primarily in the uncertainty introduced by true oceanic variability from the daily to the interannual. Significant improvements in the present numbers will occur only through the use of data sets permitting true temporal averaging of the oceanic circulation. For instance, the present solution has large uncertainties due to undersampling of the highly variable Brazil current and Pacific–Indian throughflow. Additional observations there would greatly improve accuracy. Further refinement of the a priori error estimates by using improved numerical models and other data sets (such as altimetry) is also possible. □

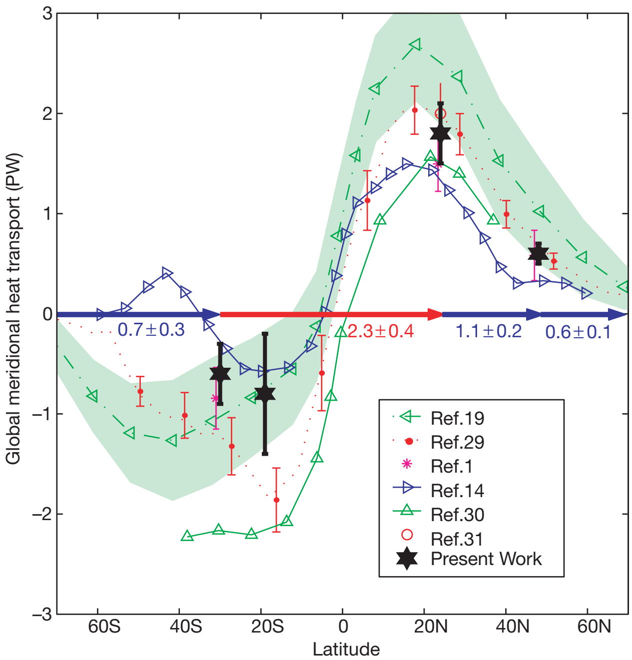

Figure 3 Global meridional heat transports. The black stars with thick error bars indicate the global, zonally integrated heat transports. Ocean–atmosphere heat exchanges between selected latitudes are given by numbers above the northward pointing arrows (positive for oceanic heating). The uncertainties from ref. 19 are indicated by the green band. The previous estimate of ref. 1 is different, but statistically consistent. No incompatibility is found between the estimates by the European Centre for Medium Range Weather Forecasts and US National Center for Environmental Prediction models[14,19,29] and our new values, owing to their large uncertainties[19]. Other climatological estimates[30,31] were published without error estimates, thus precluding any quantitative comparison. The estimate of ref. 30 is taken from their experiment B. (This figure is adapted and completed from refs 1 and 30.)

Methods

The method is that of hydrographic inverse box models[23], where the relative, geostrophic velocity field is obtained from temperature and salinity measurements across the sections of Fig. 1. This initial flow is uniformly adjusted at each location so that the flow satisfies near-conservation of mass, anomalies of salt, heat, and the phosphate-oxygen combination ("PO" $= 170[PO_4] + [O_2]$)[24,25] within oceanic layers defined by neutral surfaces (neutral surfaces are densities chosen so that work against gravity is minimized when following the surface, permitting global use of a single density variable[26]). Silica conservation is also required, top-to-bottom, while heat and PO are conserved only in layers that are not in contact with the surface. The surface layer is directly wind-driven (Ekman transport). Diffusive and advective exchanges between layers are determined by the model. The use of anomaly equations[27] permits, through noise subtraction, determination of diffusivities across each interface. Substantial improvements were made to the method, compared to that used in ref. 1, with, in particular, rigorous estimates of uncertainties through a determination of the a priori model error based on a simulation from the output of a quasi eddy-resolving (1/4°) ocean general circulation model[28].

Received 24 February; accepted 4 September 2000.

1. Macdonald, A. M. & Wunsch, C. An estimate of global ocean circulation and heat fluxes. *Nature* **382,** 436–439 (1996).
2. Houghton, J. T. *et al.* (eds) *Climate Change 1995* (Cambridge Univ. Press, 1996).
3. Ganachaud, A. *Large Scale Oceanic Circulation and Fluxes of Freshwater Heat, Nutrients and Oxygen.* Thesis, Massachusetts Institute of Technology, Woods Hole Oceanographic Institution, (1999).
4. Ganachaud, A., Wunsch, C., Marotzke, J. & Toole, J. The meridional overturning and large-scale circulation of the Indian Ocean. *J. Geophys. Res.* (in the press).
5. Roemmich, D. & McCallister, T. Large scale circulation of the North Pacific Ocean. *Prog. Oceanogr.* **22,** 171–204 (1989).
6. Broecker, W. S., Sutherland, S. & Peng, T.-H. A possible 20th-century slowdown of Southern Ocean deep water formation. *Science* **286,** 1132–1135 (1999).
7. Orsi, A. H., Johnson, G. C. & Bullister, J. L. Circulation, mixing and production of Antarctic Bottom Water. *Prog. Oceanogr.* **43,** 55–109 (1999).
8. Gordon, A. L., Susanto, R. D. & Ffield, A. Throughflow within the Makassar Strait. *Geophys. Res. Lett.* **26,** 3325–3328 (1999).
9. Jackett, D. R. & McDougall, T. J. A neutral density variable for the world's oceans. *J. Phys. Oceanogr.* **27,** 237–263 (1997).
10. Munk, W. & Wunsch, C. The Moon and mixing: abyssal recipes II. *Deep-Sea Res. I* **45,** 1977–2010 (1998).
11. Polzin, K. L., Toole, J. M., Ledwell, G. R. & Schmitt, R. W. Spatial variability of turbulent mixing in the abyssal ocean. *Science* **276,** 93–96 (1997).
12. Toggweiler, J. R. & Samuels, B. On the ocean's large-scale circulation near the limit of no vertical mixing. *J. Phys. Oceanogr.* **28,** 1832–1852 (1998).
13. da Silva, A., Young, C. & Levitus, S. *Atlas of Surface Marine Data* Vol. 1, *Algorithms and Procedures* (NOAA Atlas NESDIS 6, US Dept of Commerce, 1994).
14. Garnier, E., Barnier, B., Siefridt, L. & Béranger, K. Investigating the 15-year air-sea flux climatology from the ECMWF reanalysis project as a surface boundary condition for ocean models. *Int. J. Climatol.* (in the press).
15. Manabe, S. & Stouffer, R. J. Two stable equilibria of a coupled ocean-atmosphere model. *J. Clim.* **1,** 841–866 (1988).
16. Marotzke, J. in *Decadal Climate Variability, Dynamics and Predictability* (eds Anderson, D. L. T. & Willebrand, J.) Vol. I, 44 (NATO ASI/Springer, 1996).
17. Gleckler, P. J. & Weare, B. C. Uncertainties in global ocean surface heat flux climatologies derived from ship observations. *J. Clim.* **10,** 2764–2781 (1997).
18. Josey, S. A., Kent, E. C. & Taylor, P. K. New insights into the ocean heat budget closure problem from analysis of the SOC air-sea flux climatology. *J. Clim.* **9,** 2856–2880 (1999).
19. Keith, D. W. Meridional energy transport: uncertainty in zonal means. *Tellus* **47,** 30–44 (1995).
20. Ganachaud, A. & Wunsch, C. Oceanic nutrient and oxygen fluxes during the World Ocean Circulation Experiment and bounds on export production. *Glob. Biogeochem. Cycles* (submitted).
21. Macdonald, A. The global ocean circulation: a hydrographic estimate and regional analysis. *Prog. Oceanogr.* **41,** 281–382 (1998).
22. Schmitz, W. J. Jr & McCartney, M. S. On the North Atlantic circulation. *Rev. Geophys.* **31,** 29–49 (1993).
23. Wunsch, C. *The Ocean Circulation Inverse Problem* 437 (Cambridge Univ. Press, 1996).
24. Anderson, L. A. & Sarmiento, J. L. Redfield ratios of remineralization determined by nutrient data analysis. *Glob. Biogeochem. Cycles* **8,** 65–85 (1994).
25. Broecker, W. S. "NO", a conservative water-mass tracer. *Earth Planet. Sci. Lett.* **23,** 100–107 (1974).
26. McDougall, T. Neutral surfaces. *J. Phys. Oceanogr.* **17,** 1950–1964 (1987).
27. McDougall, T. J. in *Parameterization of Small-Scale Processes, Hawaiian Winter Workshop Aha Hulikoa* 355–386 (Univ. Hawaii, Manoa, 1991).
28. Stammer, D., Tokmakian, R., Semtner, A. & Wunsch, C. How well does a 1/4° global circulation model simulate large scale oceanic observations? *J. Geophys. Res.* **101,** 25779–25811 (1996).
29. Trenberth, K. E. & Solomon, A. The global heat balance; heat transports in the atmosphere and ocean. *Clim. Dyn.* **10,** 107–134 (1994).
30. de las Heras, M. & Schlitzer, R. On the importance of intermediate water flows for the global ocean overturning. *J. Geophys. Res.* **104,** 15515–15536 (1999).
31. Bryden, H. L., Roemmich, D. H. & Church, J. A. Ocean heat transport across 24° N in the Pacific. *Deep-Sea Res.* **38,** 297–324 (1991).

Acknowledgements

This work was completed while A.G. was a graduate student in the MIT/WHOI Joint Program in Physical Oceanography. We thank J. Toole, B. Warren, J. Marotzke, D. Glover and N. Hogg. B. Arbic, G. McKinley, A. Czaja, A. Macdonald, J. Marshall and M. Fieux also provided helpful comments on the manuscript. We are grateful to the principal investigators who provided the data from the World Ocean Circulation Experiment and the Franco-Indonesian Java-Australia Dynamic Experiment. G. Brown and D. Spiegel helped to design the figures. We were supported by the Jet Propulsion Laboratory and by gifts from Ford, General Motors and Daimler-Chrysler to MIT's Climate Modelling Initiative. This work is a contribution to the World Ocean Circulation Experiment.

Correspondence and requests for materials should be addressed to A.G. (e-mail: ganacho@ifremer.fr).

The use of earthquake rate changes as a stress meter at Kilauea volcano

James Dieterich*, **Valérie Cayol†*** & **Paul Okubo‡**

* *US Geological Survey, Menlo Park, California 94025, USA*
† *Université B. Pascal, Clermont Ferrand, France*
‡ *Hawaiian Volcano Observatory, US Geological Survey, Hawaii 96718, USA*

Stress changes in the Earth's crust are generally estimated from model calculations that use near-surface deformation as an observational constraint. But the widespread correlation of changes of earthquake activity with stress[1–5] has led to suggestions that stress changes might be calculated from earthquake occurrence rates obtained from seismicity catalogues. Although this possibility has considerable appeal, because seismicity data are routinely collected and have good spatial and temporal resolution, the method has not yet proven successful, owing to the non-linearity of earthquake rate changes with respect to both stress and time. Here, however, we present two methods for inverting earthquake rate data to infer stress changes, using a formulation for the stress- and time-dependence of earthquake rates[6]. Application of these methods at Kilauea volcano, in Hawaii, yields good agreement with independent estimates, indicating that earthquake rates can provide a practical remote-sensing stress meter.

The inversions use a formulation for earthquake rate changes[6] derived from laboratory observations of rate- and state-dependent fault strength[6–8], which constrain the earthquake nucleation process to be dependent on both time and stress. Previously, this formulation has been applied to model the spatial and temporal characteristics of earthquake clustering phenomena, including foreshocks and aftershocks[6,7], and to evaluate earthquake probabilities following large earthquakes[9]. The effectiveness of the formulation for forward modelling of earthquake phenomena, and its derivation from observed fault properties, provide the basis for its use to estimate stress changes from earthquake rate data. This approach yields stresses that drive the earthquake process. As such, it is distinct from other seismological methods that yield measures of stress changes resulting from earthquakes.

The formulation of Dieterich[6] for rate of earthquake activity R (in a specified magnitude range) can be written in the condensed form

$$R = \frac{r}{\gamma \dot{S}_r}, \text{ where } d\gamma = \frac{1}{A\sigma}[dt - \gamma dS] \qquad (1)$$

where γ is a state variable, t is time, and S is a modified Coulomb stress function defined below. The constant r is the steady-state earthquake rate at the reference stressing rate $\dot{S}_r$. A is a dimensionless fault constitutive parameter with values usually in the range 0.005–0.015 (refs 6–8). The modified Coulomb stress function is defined as

$$S = \tau - [\mu - \alpha]\sigma \qquad (2)$$

where τ is the shear stress acting across fault planes that generate earthquakes (positive in the slip direction), σ is the normal stress (less pore fluid pressure), μ is the coefficient of fault friction and α is a constitutive parameter[6,10] with an assigned value in this study of 0.25 (refs 6, 10). In equation (1), the term $A\sigma$ is a constant (that is, changes in σ are negligible relative to total σ). For a stress step, equation (1) yields the characteristic aftershock sequence, which consists of an immediate jump of seismicity rate followed by decay that obeys the Omori t^{-1} aftershock decay law with aftershock duration $t_a = A\sigma/\dot{S}$ (ref. 6).

We use two methods to estimate stress changes from earthquake rate data. The first gives stress as a function of time in a specified volume. From equation (1), the observed rate R is used to directly calculate γ as a function of time (that is, $\gamma(t) = r/R(t)\dot{S}_r$). This requires an estimate of $\dot{S}_r$, which can be obtained from independent

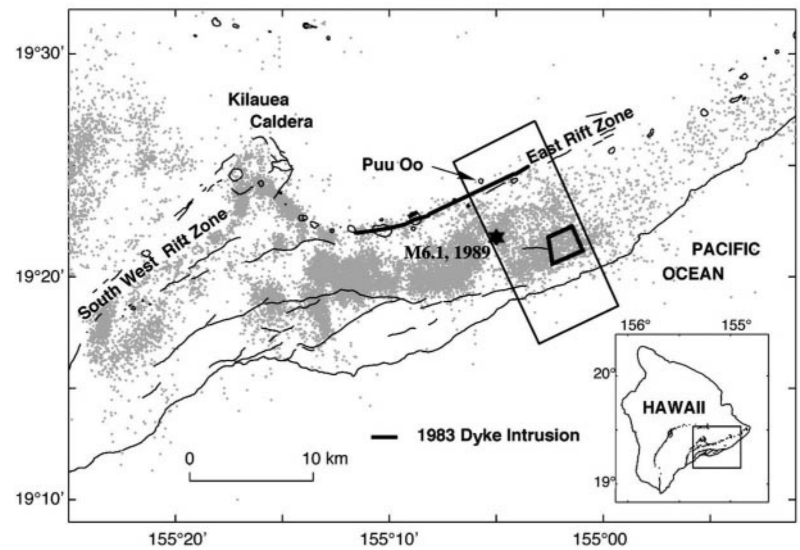

Figure 1 Map of Kilauea volcano showing earthquakes of magnitude $M \approx 1.5$ from 1976 to 1983. Intrusion of magma into the southwest and east rift zones of Kilauea causes rift expansion, and results in motion of the south flank to the SSE. Eruptive fissures initiated the Puu Oo eruption, which started 1 January 1983 and continues to the present. The small polygon is the region of analysis of Fig. 2; the large rectangle gives the region of analysis of Figs 3 and 4.

is less than 100%). Models for the additional oligonucleotide, GTP molecules and Mg^{2+} ions, have been fitted into electron density maps and refinement of these oligo–Mn^{2+}–polymerase and oligo–GTP–Mg–Mn–polymerase complexes against their data sets, imposing strict threefold NCS constraints, resulted in models with R factors of 23.7 and 21.4%, respectively, and good stereochemistry (Table 1).

Figures

Unless otherwise stated figures were drawn using BOBSCRIPT[26] and rendered with RASTER3D[27].

Received 2 August; accepted 28 December 2000.

1. Reinisch, K. M., Nibert, M. L. & Harrison, S. C. Structure of the reovirus core at 3. 6 Å resolution. *Nature* **404,** 960–967 (2000).
2. Grimes, J. M. *et al.* The atomic structure of the bluetongue virus core. *Nature* **395,** 470–478 (1998).
3. Makeyev, E. V. & Bamford, D. H. Replicase activity of purified recombinant protein P2 of double-stranded RNA bacteriophage ϕ6. *EMBO J.* **19,** 124–133 (2000).
4. Butcher, S. J., Makeyev, E. V., Grimes, J. M., Stuart, D. I. & Bamford, D. H. Crystallization and preliminary X-ray crystallographic studies on the bacteriophage ϕ6 RNA-dependent RNA polymerase. *Acta Crystallogr. D* **56,** 1473–1475 (2000).
5. Mindich, L. Reverse genetics of dsRNA bacteriophage ϕ6. *Adv. Virus Res.* **53,** 341–353 (1999).
6. Gottlieb, P., Strassman, J., Quao, X., Frucht, A. & Mindich, L. In vitro replication, packaging, and transcription of the segmented, double-stranded RNA genome of bacteriophage ϕ6: studies with procapsids assembled from plasmid-encoded proteins. *J. Bacteriol.* **172,** 5774–5782 (1990).
7. Mindich, L. Precise packaging of the three genomic segments of the double-stranded-RNA bacteriophage ϕ6. *Microbiol. Mol. Biol. Rev.* **63,** 149–160 (1999).
8. Makeyev, E. V. & Bamford, D. H. The polymerase subunit of a dsRNA virus plays a central role in the regulation of viral RNA metabolism. *EMBO J.* **19,** 124–133 (2000).
9. Ollis, D. L., Kline, C. & Steitz, T. A. Domain of E. coli DNA polymerase I showing sequence homology to T7 DNA polymerase. *Nature* **313,** 818–819 (1985).
10. Delarue, M., Poch, O., Tordo, N., Moras, D. & Argos, P. An attempt to unify the structure of polymerases. *Protein Eng.* **3,** 461–467 (1990).
11. Lesburg, C. A. *et al.* Crystal structure of the RNA-dependent RNA polymerase from hepatitis C virus reveals a fully encircled active site. *Nature Struct. Biol.* **6,** 937–943 (1999).
12. Ago, H. *et al.* Crystal structure of the RNA-dependent RNA polymerase of hepatitis C virus. *Struct. Fold. Des.* **7,** 1417–1426 (1999).
13. Bressanelli, S. *et al.* Crystal structure of the RNA-dependent RNA polymerase of hepatitis C virus. *Proc. Natl Acad. Sci. USA* **96,** 13034–13039 (1999).
14. Stuart, D. I., Levine, M., Muirhead, H. & Stammers, D. K. Crystal structure of cat muscle pyruvate kinase at resolution of 2. 6Å. *J. Mol. Biol.* **134,** 109–142 (1979).
15. Oh, J. W., Ito, T. & Lai, M. M. A recombinant hepatitis C virus RNA-dependent RNA polymerase capable of copying the full-length viral RNA. *J. Virol.* **73,** 7694–7702 (1999).
16. Lohmann, V., Overton, H. & Bartenschlager, R. Selective stimulation of hepatitis C virus and pestivirus NS5B RNA polymerase activity by GTP. *J. Biol. Chem.* **274,** 10807–10815 (1999).
17. Frilander, M., Poranen, M. & Bamford, D. H. The large genome segment of dsRNA bacteriophage ϕ6 is the key regulator in the in vitro minus and plus strand synthesis. *RNA* **1,** 510–518 (1995).
18. van Dijk, A. A., Frilander, M. & Bamford, D. H. Differentiation between minus- and plus-strand synthesis: polymerase activity of dsRNA bacteriophage ϕ6 in an in vitro packaging and replication system. *Virology* **211,** 320–323 (1995).
19. Huang, H., Chopra, R., Verdine, G. L. & Harrison, S. C. Structure of a covalently trapped catalytic complex of HIV-1 reverse transcriptase: implications for drug resistance. *Science* **282,** 1669–1675 (1998).
20. Zhong, W., Uss, A. S., Ferrari, E., Lau, J. Y. & Hong, Z. De novo initiation of RNA synthesis by hepatitis C virus nonstructural protein 5B polymerase. *J. Virol.* **74,** 2017–2022 (2000).
21. Yazaki, K. & Miura, K. Relation of the structure of cytoplasmic polyhedrosis virus and the synthesis of its messenger RNA. *Virology* **105,** 467–479 (1980).
22. Hendrickson, W. A. Determination of macromolecular structures from anomalous diffraction of synchrotron radiation. *Science* **254,** 51–58 (1991).
23. Brunger, A. T. *et al.* Crystallography and NMR system: A new software suite for macromolecular structure determination. *Acta Crystallogr. D* **54,** 905–921 (1998).
24. Navaza, J. AMoRe: an automated package for molecular replacement. *Acta Crystallogr. A* **50,** 164–182 (1994).
25. Laskowski, R. A., MacArthur, M. W., Moss, D. S. & Thornton, J. M. PROCHECK: a program to check the stereochemical quality of protein structures. *J. Appl. Crystallogr.* **26,** 283–291 (1993).
26. Esnouf, R. M. An extensively modified version of MolScript that includes greatly enhanced colouring capabilities. *J. Mol. Graph.* **15,** 132–134 (1997).
27. Merritt, E. A. & Bacon, D. J. in *Macromolecular Crystallography* (eds Carter, J. W. Jr & Sweet, R. M.) 505–524 (Academic, San Diego, 1997).
28. Nicholls, A., Sharp, K. A. & Honig, B. Protein folding and association: insights from the interfacial and thermodynamic properties of hydrocarbons. *Proteins* **11,** 281–296 (1991).

Supplementary information is available on *Nature*'s World-Wide Web site (http://www.nature.com) or as paper copy from the London editorial office of *Nature*.

Acknowledgements

J. Diprose and G. Sutton helped with synchrotron data collection; J. Diprose and S. Ikemizu with calculations; and R. Esnouf and K. Harlos with computing and in-house data collection. We thank the staff at the beamlines of the ESRF, SRS and APS, in particular Sergey Korolev at the APS for help with the MAD experiment. S.J.B. is a Marie Curie Fellow. J.M.G. is funded by the Royal Society and D.I.S. by the Medical Research Council. The work was supported by the Academy of Finland, the Medical Research Council and the European Union.

Correspondence and requests for materials should be addressed to D.I.S. (e-mail: dave@strubi.ox.ac.uk). Coordinates have been deposited in the RCSB Protein database under accesssion codes: 1HHS, 1HHT, 1HI0, 1HI1, 1HI8.

correction

Improved estimates of global ocean circulation, heat transport and mixing from hydrographic data

Alexandra Ganachaud & Carl Wunsch

Nature **408,** 453–457 (2000).

In this first paragraph of this paper, the uncertainty on the net deep-water production rates in the North Atlantic Ocean was given incorrectly. The correct value should have been $(15 \pm 2) \times 10^6\ m^3\ s^{-1}$. □

errata

Changes in Greenland ice sheet elevation attributed primarily to snow accumulation variability

J. R. McConnell, R. J. Arthern, E. Mosley-Thompson, C. H. Davis, R. C. Bales, R. Thomas, J. F. Burkhard & J. D. Kyne

Nature **406,** 877–879 (2000).

As the result of an editing error, the 1993–1998 aircraft-based altimetry surveys of the southern Greenland ice sheet reported by Krabill *et al.* (1999) were erroneously described as satellite-based. □

Genome sequence of enterohaemorrhagic *Escherichia coli* 0157:H7

Nicole T. Perna, Guy Plunkett III, Valerie Burland, Bob Mau, Jeremy D. Glasner, Debra J. Rose, George F. Mayhew, Peter S. Evans, Jason Gregor, Heather A. Kirkpatrick, György Pósfai, Jeremiah Hackett, Sara Klink, Adam Boutin, Ying Shao, Leslie Miller, Erik J. Grotbeck, N. Wayne Davis, Alex Lim, Eileen T. Dimalanta, Konstantinos D. Potamousis, Jennifer Apodaca, Thomas S. Anantharaman, Jieyi Lin, Galex Yen, David C. Schwartz, Rodney A. Welch & Frederick R. Blattner

Nature **409,** 529–533 (2001).

The Genbank accession number for the annotated sequence given in this paper was typeset incorrectly. The correct accession number is AE005174. □